

## Statistical correlation analysis of field-aligned currents measured by Swarm

J.-Y. Yang<sup>1,2</sup>, M. W. Dunlop<sup>1,3,4</sup>, H. Lühr<sup>5</sup>, C. Xiong<sup>5</sup>, Y.-Y. Yang<sup>6</sup>, J.-B. Cao<sup>1</sup>, J. A. Wild<sup>7</sup>,  
L.-Y. Li<sup>1</sup>, Y.-D. Ma<sup>1</sup>, W.-L. Liu<sup>1</sup>, H.-S. Fu<sup>1</sup>, H.-Y. Lu<sup>1</sup>, C. Waters<sup>8</sup>, and P. Ritter<sup>5</sup>

<sup>1</sup> Space Science Institute, School of Space and Environment, Beihang University, 100191, Beijing, China.

<sup>2</sup>Key Laboratory of Earth and Planetary Physics, Chinese Academy of Sciences, Beijing 100029, China.

<sup>3</sup>RAL\_Space, STFC, Chilton, Oxfordshire, OX11 0QX, UK.

<sup>4</sup>The Blackett Laboratory, Imperial College London, London, SW7 2AZ, UK.

<sup>5</sup>GFZ, German Research Centre for Geosciences, Telegrafenberg, 14473 Potsdam, Germany.

<sup>6</sup>The Institute of Crustal Dynamics, China Earthquake Administration, Beijing 100085, China.

<sup>7</sup>Department of Physics, Lancaster University, Lancaster, LA1 4YB, UK

<sup>8</sup>School of Mathematical and Physical Sciences, University of Newcastle, Callaghan, New South Wales, Australia.

Corresponding author: Malcolm W. Dunlop ([m.w.dunlop@rl.ac.uk](mailto:m.w.dunlop@rl.ac.uk))

### Key Points:

- For the first time, we infer the orientations of the current sheets of FACs.
- This study clearly reflects two different domains of FACs, small-scale which are time variable and large-scale which are rather stationary.
- We may find a way to obtain the information of Pi1B waves using low-earth orbit (LEO) satellites.

## 23 Abstract

24 We investigate the statistical, dual-spacecraft correlations of field-aligned current (FAC)  
25 signatures between two Swarm spacecraft. For the first time, we infer the orientations of the  
26 current sheets of FACs by directly using the maximum correlations obtained from sliding data  
27 segments. The current sheet orientations are shown to broadly follow the mean shape of the  
28 auroral boundary for the lower latitudes and that these are most well-ordered on the dusk side.  
29 Orientations at higher latitudes are less well ordered. In addition, the maximum correlation  
30 coefficients are explored as a function of MLT and in terms of either the time shift ( $\delta t$ ), or the  
31 shift in longitude ( $\delta lon$ ) between Swarm A and C for various filtering levels and choice of  
32 auroral region. We find that the low-latitude FACs show the strongest correlations for a broad  
33 range of MLT centred on dawn and dusk, with a higher correlation coefficient on the dusk-side  
34 and lower correlations near noon and midnight. The positions of maximum correlation are  
35 sensitive to the level of low-pass filter applied to the data, implying temporal influence in the  
36 data. This study clearly reflects the two different domains of FACs: small-scale (some tens of  
37 km), which are time variable and large-scale (>50 km) which are rather stationary. The  
38 methodology is deliberately chosen to highlight the locations of small-scale influences which are  
39 generally variable in both time and space. In addition, we may also have fortuitously found a  
40 way to obtain the information of Pi1B waves (pulsations with periods between 1-40 seconds).

## 41 1 Introduction

42 The Earth's field-aligned currents (FACs) are the dominant process by which energy and momentum are  
43 transported between the magnetosphere and the ionosphere-thermosphere system [e.g. *Foster et al.*, 1983;  
44 *Lu et al.*, 1998, *Yu et al.*, 2010], and therefore FACs are fundamentally important for the understanding of  
45 magnetosphere-ionosphere coupling. The upward FAC is responsible, at least in part, for the heating of  
46 the ionospheric electrons, although it is less clear whether the downward FAC cools the ionosphere  
47 [*Pitout et al.* 2015; *Wing et al.* 2015].

48 Both large- and small-scale FACs have been observed in the auroral zone extending over several degrees  
49 of magnetic latitude. Large-scale FACs (the Birkeland current system), with perturbations on spatial  
50 scales larger than 50 km at low-Earth orbit (LEO) satellite altitudes, have been described by *Iijima and*  
51 *Potemra* [1976a] in terms of 'Region 1' (R1) and 'Region 2' (R2) systems, which couple the external  
52 magnetospheric currents to the high-latitude ionosphere and the inner magnetosphere to the auroral  
53 ionosphere. *Iijima and Potemra* [1978] later found that the field-aligned currents flow into Region 1 on  
54 the dawn-side and away from Region 1 (out of the ionosphere) on the dusk-side. They also found that the  
55 current flow in Region 2 is reversed with respect to Region 1 at any given local time except in the Harang  
56 discontinuity region, ~20:00-24:00 MLT [*Harang*, 1946], where the flow patterns are more complicated.  
57 There is evidence that the large-scale FACs are generated by the 'long-term' interaction of the solar wind  
58 with the magnetosphere (for recent work, see *Wing and Johnson*, [2015], which showed upwards R1  
59 currents can be driven by solar wind velocity shears at the magnetopause), although these current sheets  
60 can often have complicated spatial and temporal variations (here 'sheet' refers to the discussion of the  
61 azimuthal extent of R1/R2 FACs in this paper). Small-scale FACs are usually characterized by quasi-  
62 equal, parallel sheets of current into and out of the ionosphere with latitudinal thicknesses of tens of km at  
63 low Earth orbit (LEO) altitudes and with typical timescales of order 10 seconds or less. These small-scale  
64 FACs are associated with 'short-lived' plasma processes within the magnetosphere such as discrete auroral  
65 arcs [*Anderson and Vondrak*, 1975], field-line resonances [*Rankin et al.*, 1999; *Pitout et al.*, 2003; *Waters*  
66 *and Sciffer*, 2008], bursty bulk flows in the plasma sheet [*Merkin et al.*, 2013; *Yu et al.*, 2017] and  
67 associated Pi2 [*Cao et al.*, 2008, 2010], as well as Pi1 waves which will be discussed in detail in section  
68 3.3.

69 Nevertheless, separation of the temporal and spatial nature of both small- and large-scale FACs has been  
 70 notoriously difficult [for example see *Lühr et al.*, 2015; *Stasiewicz et al.* 2000] since these currents are  
 71 both highly dynamic and vary in size, while single spacecraft estimates generally require assumptions of  
 72 either geometry (such as infinite sheets, as adopted by, for example, *Anderson and Vondrak* [1975];  
 73 *Marshall et al.* [1991]) or some degree of time stationarity (to apply  $dB/dt$  to a spatial estimate, where  
 74 multi-spacecraft estimates are unavailable [*Dunlop et al.* 1988], for comparison). Despite this problem,  
 75 since the first identification of FACs [*Zmuda et al.*, 1966; 1967; *Iijima and Potemra*, 1976a], many  
 76 previous, typically statistical, studies have been performed, using single and multi- spacecraft methods  
 77 (see *Higuchi and Ohtani* 2000), or indirect observations, to probe their global natures [e.g. *Anderson et*  
 78 *al.*, 2000; *Gjerloev et al.*, 2011; *Dunlop et al.*, 2015a,]. An investigation of the characteristics of FACs  
 79 which are restricted in both their spatial and temporal variations between multiple spacecraft positions has  
 80 also recently been carried out by *Forsyth et al.*, [2017] (through the development of a rigorous test of  
 81 purely static, 1-D normal current sheets) and has been applied recently in a study by *McGranaghan et al.*,  
 82 [2017].

83 The alignment of current sheets of large-scale FACs is generally along the boundary of the auroral oval,  
 84 but can be noticeably distorted during very disturbed periods [*Iijima and Potemra*, 1978]. Nevertheless, it  
 85 has been argued that the basic pattern may often be maintained [*Gjerloev and Hoffman*, 2014], although  
 86 the intensity of currents varies from event to event. Here, we have used the recently acquired Swarm  
 87 multi-spacecraft data set to investigate the MLT dependence of the correlations between the two  
 88 spacecraft field-aligned current sheets with a new method using statistical analysis of the inter-spacecraft  
 89 maximum correlations between FAC signatures, which also shows directly the auroral alignments of the  
 90 current sheets. The sensitivity of this analysis to the filtering of the data and both the time delay and  
 91 longitudinal separation between the spacecraft are explored. The statistical work shows differences  
 92 between large-scale FAC sheets which occur mainly in the dawn- and dusk- sectors and more localised  
 93 current sheets possibly associated with the NBZ [as defined by *Iijima et al.*, 1984] and cusp currents  
 94 [*Iijima and Potemra* 1976b], also referred to as Region 0 currents [*Bythrow, et al.*, 1988].

## 95 **2 Methodology**

96 The Swarm mission [*Friis-Christensen et al.* 2008] consists of three spacecraft (A, B and C) flying in  
 97 phased, circular, low-Earth polar orbits since launch on 22 November 2013. The data set used here was  
 98 mainly the FAC signals derived from the Swarm A and C observations during the final constellation  
 99 phase (operations from 17<sup>th</sup> April 2014), where the two spacecraft had orbital periods of ~94 minutes,  
 100 flying side-by-side at a mean high-latitude altitude of about 470 km, and sampling all local times in about  
 101 132 days. The third spacecraft Swarm B flies at a slightly higher orbit at ~531 km altitude, with a slightly  
 102 different orbital period of ~95 minutes and drifts in MLT with respect to Swarm A and C, which remain  
 103 close together throughout the time period studied here. The three Swarm spacecraft move through the  
 104 auroral regions and across the polar cap as a result of their near polar orbits.

105 We use the official 1 Hz Level-2 OPER (Routine Operations of file class) FAC data taken from the  
 106 Vector Fluxgate Magnetometer (VFM) [*Friis-Christensen et al.*, 2008, *Ritter et al.*, 2013, *Stolle et al.*,  
 107 2013] on Swarm. To minimize the non-linear variation of the magnetic field gradients, these data are  
 108 processed by initial subtraction of the model “mean field” (the core, crustal and magnetospheric fields at  
 109 the satellite altitude) to obtain the residual data [see *Dunlop et al.*, 2015b]. This generally results in a 5%  
 110 uncertainty [*Ritter et al.*, 2013] in the estimates of the FACs as a result of non-physical errors. These  
 111 estimates are provided as part of the standard Swarm level 2 data products  
 112 (<https://earth.esa.int/web/guest/swarm/data-access>) with a cadence of 1 second and are obtained using a  
 113 single-spacecraft method assuming that an infinite (1-D) current sheet approximation applies locally to  
 114 each spacecraft (i.e. that the local structure sampled is approximately a planar sheet on temporal and  
 115 spatial scales which are consistent with the 1 sec cadence). Here we also apply a low pass filter to this 1  
 116 second data with both 20 and 60 second cut-offs (removing higher frequency signals and maintaining

117 cadence) to obtain the large-scale (i.e. 150/450 km; corresponding to 20/60 second cut-offs respectively)  
 118 FAC data. This filtering also serves to clarify the inter-comparison of spacecraft A and C data, which  
 119 have a spatial separation of  $\sim 150$  km (see discussion below). For our presentations in magnetic latitude  
 120 and MLT we use APEX coordinates [Richmond, 1995] throughout. To probe the duration and extent of  
 121 the FAC sheets, especially in different MLT regions, we statistically analyse the correlations between  
 122 FACs observed by Swarm A and C during the period 17<sup>th</sup> April 2014 to 30<sup>th</sup> April 2016 when both  
 123 spacecraft were flying side-by-side with apex longitude difference less than 3 degrees and a lagging time  
 124 (from one spacecraft to the other) less than 20 seconds. Latitude is considered only through the auroral  
 125 region (see below).

126 Figure 1 demonstrates the method we have adopted for data selection and the correlation analysis. Figures  
 127 1(a) and 1(b) show FACs along several Swarm orbit tracks within time period of 09:29-20:31 UT on 6<sup>th</sup>,  
 128 June, 2014, projected onto APEX coordinates. We can see that similar FAC signals on Swarm A and C  
 129 were seen for several hours, revealing corresponding current sheets distributed over some longitudes, but  
 130 slowly changing in time and orbit track. Although the signals observed by Swarm A and C are very  
 131 similar, differences are observed between them, even though the time delay for each spacecraft to arrive  
 132 at the same APEX latitude varies from a few to about 14 seconds, and the difference in longitude ( $\delta lon$ ) is  
 133  $\sim 1$ -3 degrees between Swarm A and C. The total time difference between the dual-spacecraft segments of  
 134 maximum correlation (bold orbit segments in Figure 1c-f), indicates the time difference of arrival at the  
 135 same current sheet,  $\delta t$  (see below).

136 To obtain the correlations of FACs observed by the two satellites we separate the regions between the  
 137 modelled poleward and equatorward auroral boundaries (as defined by the method of Xiong and Lühr,  
 138 [2014]) into two broadly equal intervals predominantly containing ‘R1’ and ‘R2’ signals (each containing  
 139 approximately the same range of latitudes). The modelled poleward and equatorward auroral boundaries  
 140 on 14:30 UT 6<sup>th</sup> June 2014 are shown in Figure 1 (a, b) by the magenta dashed curves. In Figure 1(c-f),  
 141 however, for each orbit track the specific auroral boundaries are indicated by vertical dashed lines. The  
 142 effective total time shift ( $\delta t$ ) and the longitude difference ( $\delta lon$ ) between the two spacecraft when the  
 143 positions of the maximum correlations are found are denoted in each panel. Maximum correlations are  
 144 obtained for 60 second sliding orbit segments of Swarm A and C within the R1 or R2 intervals. The  
 145 segments with maximum correlation adopted finally are shown in Figure 1(c-f) by bold traces for each  
 146 spacecraft (where the maximum correlation and longitude difference are indicated in blue text) with two  
 147 different low pass filters, 20 seconds and 60 seconds. The filtering of the data defines the optimum data  
 148 segments for that resolution and tests the temporal content, i.e. the degree of stationarity in the data signal  
 149 is expected to decrease with decreasing scale size of activity.

150 We use 60-second length segment windows for the correlation to get rid of any influence from variable  
 151 lengths on the computation of the maximum correlations. From tests using different segment lengths, we  
 152 found that using longer segments can reduce the effectiveness in finding the max-correlation between two  
 153 tracks when the ‘R1’ or ‘R2’ contain too many points within the segments, and it also can increase the  
 154 likelihood of non-regular, shorter tracks occurring, introducing systematic errors in the maximum  
 155 correlations. On the other hand, segments with too few points can decrease the confidence level of the  
 156 correlation. After some experimentation, we selected a 60-second sliding window to maximise  
 157 correlations and minimise the effects of systematic errors. When there is less than 72 points in an orbit  
 158 track we remove the track.

159 The traces in Figure 1(c-f) show two different orbits for the correlation analysis, organized by apex  
 160 latitude. In Figure 1c, the bold traces at higher latitude are close together and the traces generally fall on  
 161 top of one another with only small-scale differences between Swarm A and C. Therefore, the large-scale  
 162 current sheet appears to be well aligned in latitude within the broad region ‘R1’. This high degree of  
 163 similarity, furthermore, also results in the maximum correlation fixing to a different orbit segment within  
 164 ‘R1’ in the case of the 60seconds filtered trace (Figure 1d), i.e. implying that the particular segments used

165 are not critical for the application of different filter windows. In the lower pair we see that the current  
 166 sheet is also well aligned at the Apex latitude for the ‘R1’ interval but not well aligned for the ‘R2’  
 167 interval (since Swarm A and C see similar profiles at different latitudes). Note that in this lower case the  
 168  $\delta lon$  is larger ( $\sim 3$  degrees), whereas the  $\delta t$  varies ( $\sim 20$  seconds for the 20s filtered trace and  $\sim 5$  seconds  
 169 for the 60s filtered trace), so that in the top pair the small differences are probably temporal whereas in  
 170 the lower pair the differences are spatial. Each example defines a particular ( $\delta lon$ ,  $\delta t$ ) for the MLT of the  
 171 orbit track. Building up the statistics allows us to study the correlation trends as a function of MLT and  
 172 the differences in APEX longitude or time between Swarm A and C, and to define an approximate  
 173 orientation of the large-scale FACs (see section 3).

### 174 3 Correlation Analysis

#### 175 3.1 Current sheet orientation

176 We can see from Figure 1(c-f) that the 2 orbits chosen show distinct situations. The first shows a time  
 177 delay of  $\sim 13$  seconds between Swarm A and C, with small difference in longitude, and the FAC signals  
 178 are seen at the same latitude. The second shows a different time delay in a different region (which  
 179 changes for different filters), together with a larger difference in longitude. Figure 1 (e-f) shows a time  
 180 delay in R1 of 12 seconds, and in R2 of 20 seconds (for 20s filtered data) and 5 seconds (for 60s- filtered  
 181 data). The reason for different time delays (20 seconds in Figure 1e and 5 seconds in Figure 1f in R2) is  
 182 that the maximum correlations appear at different latitudes when using different low pass filters, which  
 183 select different temporal, and hence spatial, scales. If we draw a line between the centres (average  
 184 positions) of the two orbit segments which give the maximum correlation between Swarm A and C, then  
 185 this provides an estimate of the orientation of the current sheet. Inevitably there are influences arising  
 186 from any temporal evolution of the current sheet between Swarm A and C (depending on the filtering  
 187 used [Lühr *et al* 2015; Forsyth *et al.*, 2017]), such as influence arising from any propagation of the  
 188 current sheet during the shifted time,  $\delta t$ . In addition, spatial structure on the scale of the spacecraft  
 189 separation will also influence the estimate [Dunlop *et al.* 2016, 2018]. Nevertheless, the important point  
 190 to note here is that for high levels of cross-correlation and hence for large-scale structures which do not  
 191 significantly evolve on the scale of  $\delta t$  and  $\delta long$ , the estimates are more accurate, so that fluctuations and  
 192 variance in the orientations highlight the presence of small-scale FACs. From statistics, we find that the  
 193 20s and 60s filtered data show very similar results. Thus, these current sheet orientations of R1 and R2 at  
 194 110 km altitude are drawn on polar maps in Figure 2a and 2b only for the 20 second filtered dataset.

195 It needs to be pointed out that, as mentioned earlier, we use the model estimated auroral boundaries from  
 196 Xiong and Lühr [2014] here to split each auroral track into two regions, and indicate them as higher  
 197 latitude regions (labelled loosely as ‘R1’ in this paper) and lower latitude regions (labelled approximately  
 198 as ‘R2’ in this paper). Since we are using only these broad definitions of the intervals for simplicity, we  
 199 expect that the ‘R1’ set actually contains other currents than purely R1, and that the ‘R2’ set contains  
 200 some R1 currents in actuality, and indeed there are other currents around noon. Nevertheless, from a  
 201 statistical perspective we expect that the main characteristics of the large-scale currents will dominate  
 202 each region. The polarity of the currents in R1/R2 also does not affect our results since we are considering  
 203 only the ordering of the current sheet orientations (and the pattern of correlations with MLT in section  
 204 3.2).

205 Figure 2a,b show inferred current sheet orientations (estimated by the method described above and as  
 206 described in the caption) for each region using 20 seconds filtered data from 17<sup>th</sup> Apr. 2014 to 20<sup>th</sup> Aug.  
 207 2014, during which time period the Swarm A and C orbits have covered the Earth for nearly a full range  
 208 of 24 hrs LT. Figure 2a, denoted by ‘R1’, shows the current sheet orientations found for the higher  
 209 latitude regions. Figure 2b, denoted by ‘R2’, is for the lower latitude regions. The magnitude of the  
 210 longitudes ( $0^\circ$ ,  $90^\circ$ ,  $180^\circ$  and  $-90^\circ$ ) in Apex coordinates are denoted on each figure and the latitudes  
 211 in the same coordinates are denoted at the line of  $135^\circ$  longitude. The sets of line segments shown in

212 each panel, representing the current sheet orientations, are drawn for those estimates at correlation values  
213 over 0.97. At this threshold the patterns are most clearly visible and show the distinction in the ordering  
214 in each region (see below). For lower threshold values of the correlation more vectors would be included  
215 and these contain more influence from temporal and spatial effects.

216 The implication of Figure 2b is that the large-scale current sheets in the lower latitude region broadly  
217 follow the oval on the dusk side and also are well consistent (although slightly less well ordered) with the  
218 oval pattern on the dawn-side. In the dawn-dusk regions, therefore, this ordering of the current sheets is  
219 very apparent and appears to be more significant on the dusk side oval. Near noon in particular, however,  
220 the current sheet orientations are more randomised and perhaps reflect the influence from other current  
221 systems in that region and/or smaller scale structures. It also appears that the alignment of the current  
222 sheets is better ordered as we move to the lowest latitudes in the distribution. Figure 2a shows that the  
223 orientation of the current sheets for the higher latitude region is less well ordered to the oval. This  
224 suggests that the character of the poleward current sheets is less dominated by large-scale structures and  
225 that this region contains more than one current system.

226 As a further check on the stability of these estimates, Figure 2c shows the comparison of these current  
227 sheet orientations to those implied for a 1-D current sheet inferred from maximum variance estimates  
228 (MVA, see *Sonnerup and Scheible*, [1998]) of the orientations in terms of the intersection angle (the  
229 difference between the orientations for each method). The data segments for MVA were taken from those  
230 used for the maximum correlations for each Swarm A position. The current sheet orientations obtained  
231 from maximum correlation are quite similar to the estimates using the MVA method. The plot shows that  
232 the intersection angles of the average current alignments derived from these two methods (MVA and  
233 maximum correlation) for Swarm A and C data from 17<sup>th</sup> Apr. 2014 to 30<sup>th</sup> Apr. 2016 and these are all  
234 less than 0.8 deg (and less than this in the auroral region). The intersection angles are lowest in the dawn  
235 side region. In fact, the difference between the two methods will arise naturally since the MVA  
236 measurement is centred on the Swarm A position whereas the maximum correlation result is an average  
237 centring on a position midway between A-C. We might expect that these will agree best in regions  
238 dominated by large-scale structure and this is indeed the case although there is an asymmetry in the extent  
239 of the agreement from dawn to dusk. The close agreement on the dawn side suggests that the orientations  
240 from both methods on the dawn side are more stable over a wider range of MLT and that the effect of the  
241 differing positions is less, perhaps due to the simpler shape of the oval on the dawn-side. On the other  
242 hand, the close average alignment of the maximum correlation orientations on the dusk side suggests that  
243 the large-scale ordering is most dominant there. Such asymmetric character from dawn to dusk is also  
244 seen in the correlation trends discussed below.

245 Figure 2d, denoted by 'R1&R2', shows the current sheet orientations for both the higher and lower  
246 latitude regions combined, superimposed on the average distribution of FACs for Swarm A from 17<sup>th</sup> Apr.  
247 2014 to 30<sup>th</sup> Apr. 2016. In the underlying pattern of FACs we see the Region 2 and Region 1 up-down (in  
248 the field-aligned sense this corresponds to: negative-positive) currents as well as the Region 0 and NBZ  
249 regions near noon. This overlay plot shows that the current sheet orientations of 'R1&R2' can cover the  
250 whole oval region, as well as the Region 0 and NBZ region. The alignment of the current sheets reflects  
251 the large-scale features in the polar map of average FACs closely. Although further work is required to  
252 quantify the characteristics, the mean position separating of Region 1 and Region 2 can be seen. In  
253 addition, the cluster of differing orientations near noon corresponds to the average currents seen there.  
254 The intensity of the average current does not correlate with the alignment of the sheets in general.

255 Further details of the FAC current sheet orientations (in particular, separating the behaviour in terms of  
256 activity and other external drivers and exploring further the stability of the orientations for different  
257 correlation levels) will be discussed in future work. Here, we focus simply on the R1/R2 alignment in  
258 order to compare with the correlation trends described below.

### 259 3.2 Correlation trends

260 Using the methodology described in section 2 we analysed the data from 17<sup>th</sup> Apr. 2014 to 30<sup>th</sup> Apr. 2016,  
261 where the spacecraft pair A-C covered a close range of both cross-track (local time longitude,  $\delta lon$ ) and  
262 along track (time differences between the spacecraft,  $\delta t$ ) positions (see Figure 1). The range of  $\delta t$  and  $\delta lon$   
263 are 0-0.3 minutes along track and 0-3 degree longitude (APEX coordinates) across track. These ranges  
264 allow us to separate the cross correlations between the spacecraft into both  $\delta t$  and  $\delta lon$  bins  
265 independently, so as to explore the MLT dependence of the correlations. We have explored these  
266 correlations for both filtered and unfiltered data to understand the effect of large- (>150 km) and small-  
267 (~7.5 km) scale structures, and their trends. The filtered data, as discussed earlier, allows consistent  
268 comparisons on the scales of the inter-spacecraft separation (i.e. ~150 km) and above. The lower choice  
269 of 20 secs matches the cadence used for the dual spacecraft FAC product in the Swarm level 2 data and  
270 therefore was used for the estimates of current sheet orientation in the previous section. It should be  
271 emphasised that it is not always possible to completely separate spatial and temporal behaviour and small-  
272 scale FACs in general depend both on space and time. Nevertheless, single spacecraft FAC estimates can  
273 still be valid locally at each spacecraft within certain criteria [Lühr *et al.* 1996] and the Swarm products  
274 are calculated at the higher smoothed cadence of 1 sec (what we term unfiltered data here). Although  
275 some types of behaviour are problematic, and the estimates can be quantitatively in error, variations on  
276 the spacecraft separation scale can be monitored through their effect on the correlation trends. We use the  
277 single spacecraft estimates in this sense here to reveal the locations and some characteristics of the  
278 smaller scale currents, through comparison of filtered and unfiltered signals.

279 Figures 3a and 3b show two 3×3 arrays of MLT trends separated by regions as described in section 2. For  
280 ‘R1&R2’ the analysis is performed across the whole interval, rather than for the separated ‘R1’ and ‘R2’  
281 intervals. These intervals are chosen to capitalize predominantly Region 1 and 2 signals separately. We  
282 expect that the R2 interval should relate to actual region-2 FACs but also contain some actual R1 currents,  
283 even some other currents at noon, as shown by Figure 2b. Meanwhile the R1 interval will include many  
284 of the other high latitude current systems from time to time. It is instructive to consider this separation for  
285 both unfiltered and filtered data. Figure 3a shows the trends with respect to the time delay from the  
286 Swarm A and C spacecraft. The top panels of Figure 3a show the total correlations for the unfiltered  
287 magnetic residuals, i.e. those including signals from both small and large-scale structures. The panels  
288 headed ‘R1’ and ‘R2’ show clearly distinct trends in both MLT and  $\delta t$ ,  $\delta lon$ , which actually are broadly  
289 maintained for each of the filtered datasets, consistent with the predominant nature of these regions. The  
290 R1&R2 panel is shown for context and represents the strongest effect of the signals seen in the whole  
291 auroral and some of the polar regions.

292 For the unfiltered, 1s resolution data, the R2 correlations remain relatively high for a broad range of MLT  
293 and are obviously lower for the range 9-15 MLT (i.e. around local noon). There is also a minor dip in the  
294 strength of the correlations from 0-3 MLT (i.e. at local midnight). This trend is maintained for most of the  
295 range of  $\delta t$  and is consistent with the expectation that R2 FACs are stable for a large range of MLT,  
296 centred on pre-dawn and post-dusk. The correlations on the dusk-side are higher, and extend for the  
297 maximum range of  $\delta t$ , suggesting a dawn-dusk asymmetry in the stability of R2 FACs. This is probably  
298 associated with the high correspondence between particle precipitation at dusk and R2 FACs (see Korth *et*  
299 *al.*, [2014]). By contrast, the R1 correlations peak during the ranges 15-21 MLT and 3-9 MLT, i.e. dusk  
300 and dawn, and are maintained for a smaller range of  $\delta t$ . Thus, the correlations are lower (less than 0.83)  
301 for a broad range of MLT around local midnight. These R1 correlations also peak at  $\delta t$  near 0.13 mins, or  
302 8 seconds, which may indicate that Pi1B waves [e.g., Heacock 1967; Arnoldy *et al.*, 1998] probably can  
303 be revealed by LEO satellite by this method. This will be discussed in section 3.3). These trends are  
304 consistent with the expectation that R1 FACs will be more temporally unstable overall and there is some  
305 indication that at either side of noon the signatures are more stable: the lower correlation around noon is  
306 possibly a result of the presence of other FACs, such as the NBZ currents or Region 0 currents which also  
307 are called cusp currents. The fact that the higher correlations extend away from noon is consistent with  
308 the average dawn-dusk signature of R1 currents, while the minimum post-midnight may be consistent

309 with the presence of the diffuse aurora, which is most likely composed of field-aligned plasma sheet  
 310 electrons scattered by the very low frequency (VLF) whistler-mode chorus waves [Wing *et al.*, 2013] and  
 311 see the suggestions of *Newell et al.*, [2009], *Korth et al.*, [2014], or *McGranaghan et al.*, [2016].

312 The 20 secs and 60 secs filtered data shows similar trends, but a higher value of correlations, to those for  
 313 R1 and R2 separately. This appears to suggest that the medium to large-scale FACs dominate the MLT  
 314 trends, but other work has indicated this may not always be the case [*Neubert and Christiansen*, 2003;  
 315 *McGranaghan et al.*, 2017]. We see, moreover, that the combined region R1&R2, for 20 secs filtering  
 316 maintains the combined distribution, suggesting that it is the smaller scale currents which affect the loss  
 317 of correlation in the unfiltered data. Broadly, the trends with MLT for R1 and R2 are more similar for the  
 318 filtered data to each other, peaking away from both noon and midnight. This is consistent with the general  
 319 pattern of large-scale FACs for both R1 and R2, which follow the well-known upward and downward  
 320 pattern for a broad range of local times surrounding dawn and dusk (*Iijima and Potemra* 1978). However,  
 321 the 20 secs and 60 secs filtered data for R1 shows some additional structure, i.e. the correlations  
 322 sometimes (e.g., at 15-18 MLT for 20 secs and 18-21 MLT for 60 secs filtered data) increase instead of  
 323 decrease as  $\delta t$  decrease at the lowest  $\delta t$  (0-0.05 min bins). This implies the trend modulated by the wave  
 324 is defeated by the expected peak at low  $\delta t$ , which is an obvious trend for the unfiltered correlation in  
 325 Figure 3c.

326 The trends in Figure 3b are shown for the  $\delta lon$  separation between Swarm A and C, which are different  
 327 from the trends for  $\delta t$ . Firstly, we see that the R1 trends are highly localised to small  $\delta lon$  (0-0.5 degs)  
 328 and rapidly fall off as  $\delta lon$  increases. The correlations of the two highest correlated, or steadier, FACs  
 329 regions, 15-21 and 3-9 MLT for R1, fall from about 0.94 to 0.78, for the unfiltered data, and ~0.995 to  
 330 ~0.975 for the filtered data. This suggests that the FAC profiles are very sensitive to shifts in longitude.  
 331 This effect lessens significantly for the 20 secs and 60 secs data, as might be expected for larger scale  
 332 FACs. This can be attributed to the lower applicability of the infinite current sheet approximation to the  
 333 small-scale currents. This also suggests that the correlations seen in  $\delta t$  are dominated by the periods when  
 334 A-C have a small difference in longitude.

335 R2 currents exhibit similar but weak trends. After examining the number of cases in each bin, we suggest  
 336 the peaks around  $\delta lon \sim 1$  degree are probably from the rare cases in the lowest of all valid bins  
 337 (containing not less than 5 cases). The higher correlations and less sensitive to shifts in longitude in 'R2'  
 338 region for the 20 secs data revealed by Figure 2b is consistent with the more aligned current sheets.

339 We have also investigated the combined correlations between spacecraft pair A-B and B-C. The range of  
 340  $\delta t$  and  $\delta lon$  are much higher than those of spacecraft pair A-C, because of the distinct orbit of 'B'. Figure  
 341 3c is similar to Figure 3a but shows  $\delta t$  in the range of 0-44 minutes along track with data limited by  
 342  $\delta lon < 10$  degrees. Figure 3d is similar to Figure 3b but shows a  $\delta lon$  of 0-15 degree across track with data  
 343 limited by  $\delta t < 30$  min. The MLT dependence can still be found, with correlations higher at the dawn and  
 344 dusk side for both R1 and R2, but is a little more night-ward for R2. The unfiltered data shows that the  
 345 correlations decrease as  $\delta t$  increases, but this trend is not so clear for the filtered data. Figure 3d reveals  
 346 only the MLT dependence of both filtered and unfiltered data but no obvious trend by different  $\delta lon$ . This  
 347 may be because of the influence from different altitudes of each spacecraft, i.e. 470km, versus 531km, which  
 348 compete with the  $\delta t$  or  $\delta lon$  sensitivity. However, it can probably confirm that the large-scale R1/2 FACs  
 349 are relatively stable in tens of minutes, otherwise the lower two panels of Figure 3c should exhibit some  
 350 descending trend with  $\delta t$ .

351 The  $\delta t$  versus  $\delta lon$  dependence of correlations taken at different MLT regions (not shown here)  
 352 demonstrates that the peak in  $\delta t$  seen for 'R1', corresponding to temporal variations of order ~8 seconds  
 353 (as outlined above), doesn't come from a specific low  $\delta lon$  by chance. This probably suggests that the  
 354 modulation of the currents by Alfvén waves is notable in the 'R1' region [*Ma et al.*, 1995; *Stasiewicz et*

355 *al.*, 2000; *Liu et al.*, 2009]. In fact, we see that for the unfiltered combined interval R1&R2, nearly only  
 356 the overlapping region between 18-21 MLT remains high (more than 0.85), and is also centred around  $\delta t$   
 357  $\sim 0.13$ mins (8 seconds). We will discuss this phenomenon in detail in section 3.3.

### 358 3.3 Pi1B waves

359 The occurrence of ground based Pi1B is well-documented [e.g., *Heacock* 1967; *Arnoldy et al.*, 1998].  
 360 Here ‘B’ is the abbreviation for ‘Burst’. Although there is evidence of both an ionospheric origin, there is  
 361 still no agreement on the origin of the Pi1B waves. Heacock suggested that ground Pi1B waves were not  
 362 generated in space because of the lack of frequency dispersion in the ground events. Subsequently,  
 363 several studies have shown the association of Pi1B waves with different types of ionospheric activity  
 364 [*Arnoldy et al.*, 1998 and papers therein] indicating that the waves probably result from ionospheric  
 365 current fluctuations. Using magnetic field data, *Arnoldy et al.*, [1998] showed that Pi1B waves observed  
 366 by the geosynchronous GOES (Geostationary Operational Environmental Satellites) satellites were nearly  
 367 simultaneously observed on the ground and appeared to be initiated by the dipolarization process of the  
 368 night-side tail magnetic field at the onset of substorms. *Arnoldy et al.* further commented that with  
 369 induction antennas sampling up to 10 Hz, there is indeed evidence of dispersion in the higher frequency  
 370 Pi1B waves.

371 Other work has also suggested that Pi1B waves are associated with substorms, as well as FACs. *Lessard*  
 372 *et al.* [2006] suggested that they were excited by reconnection or some other processes, and were  
 373 compressional in nature, at least at geosynchronous orbit, implying either fast or slow mode. It should be  
 374 noted that slow mode waves would be quickly damped so do not propagate to the ionosphere. However,  
 375 the fast mode waves can propagate isotropically, cutting across the magnetic field obliquely in the vicinity  
 376 of the GOES satellites. They noticed that at FAST (Fast Auroral Snapshot Explorer) altitudes, the waves  
 377 are of shear-mode, so must have undergone mode conversion in the region between GOES 9 and FAST.  
 378 They suggested it was possible that as the waves approached the higher latitude regions of the  
 379 magnetosphere, they gradually became increasingly parallel to the background field, where they may take  
 380 on the properties of a shear wave (a guided wave) and follow the field lines to the ionosphere. Other  
 381 models have also been suggested [*Pilipenko et al.*, 2008; *Lessard et al.*, 2011] to interpret how  
 382 propagating compressional fast magnetosonic (FMS) modes transform into running Alfvén waves.

383 Since Pi1B waves may change mode as they propagate, and are not well studied, it is important to  
 384 investigate them at different altitudes. Under normal conditions, the curl-free part of the ionospheric,  
 385 horizontal current, as well as FACs, can’t directly produce any magnetic field disturbances below the  
 386 ionosphere [*Fukushima*, 1976] and thus these currents are usually magnetically invisible on the ground,  
 387 but can be detected by satellites above the ionosphere. Therefore, although it is known that in general  
 388 ground stations usually observe Pi1B waves between 2100 and 0200 MLT [*Arnoldy et al.*, 1998, *Posch et*  
 389 *al.*, 2007], ground magnetometer data alone cannot define the ionospheric phenomena. Nevertheless, it is  
 390 hard to observe ultra-low frequency (ULF) waves in LEO satellites since a satellite generally moves fast  
 391 at this altitude so that distinguishing the temporal from the spatial variations is challenging; particularly  
 392 using single spacecraft measurements. The maximum correlation method, introduced here, however, can  
 393 give us the spatial and temporal variation of the FACs, so potentially providing information on Pi1B  
 394 properties, which are associated with the upward [*Bösinger et al.*, 1981] and downward [*Milling et al.*,  
 395 2008] FACs.

396 Figure 3 reveals apparent evidence of a correlation maximum around 8 second, which is about 0.13 Hz. In  
 397 order to clarify this, Figure 4a represents the number of cases found in each bin of Figure 3a. Even though  
 398 the data points are not equally distributed in each bin, Figure 4a only shows some overall trend for the  
 399 specific orbits of Swarm A and C. The peaks around 8 seconds are not consistent with the Figure 4a, so  
 400 do not arise from the basis time phasing between Swarm A and C (shifted by 8 seconds for orbit cross-  
 401 over). Figure 4b is another way to express the behaviour shown in Figure 3a, where the correlations are  
 402 no longer shown by colour, but by the y axis on the left of each panel. Different colours represent

403 different MLTs and the  $\delta t$  difference is now shown in the  $x$  axis. Through Figure 4b, we can see the  
404 correlation peak around 0.13 minute (about 8 second), nearly at all MLT, and most pronounced for the  
405 15-21 MLT regions. *Bösinger and Wedeken*, [1987] have mentioned that Pi1B wave enhancement at  
406 0.08–0.25 Hz was frequently observed at each of their 6 stations in both horizontal components. We note  
407 here that this is just around 4-12 second in the time domain with the centre at just 8 second, as revealed by  
408 our correlation method. In contrast to the local range in longitude of the 6 stations mentioned in their  
409 paper, the Pi1 band phenomenon revealed by the maximum correlation method here exhibits a global  
410 property and the wave character is most obvious in R1, which is considered to map mostly to the  
411 boundary plasma sheet (BPS). Additionally, the 60s filtered data of R1&R2 (the lower left panel of  
412 Figure 3a) shows another peak at around 0.26 minutes (~16 second), which can be treated as a secondary  
413 harmonic of the 8 second wave. It is reasonable that the harmonic wave appears when the data are low-  
414 pass filtered.

415 Although the Pi1B waves observed on the ground have maximum amplitude when they lie underneath  
416 active auroral forms (*Haldoupis et al.*, 1982; *Bösinger and Wedeken* 1987; *Arnold et al.*, 1998; *Danielides*  
417 *et al.*, 2001; *Milling et al.*, 2008), thereby suggesting they were locally generated [*Posch et al.*, 2007]. a  
418 number of studies have mentioned that Pi1B waves can extend in latitude and longitude/MLT (for  
419 example: 12° in latitude and 20° in longitude, as mentioned by *Arnoldy et al.*, [1998]; 7° of magnetic  
420 latitude and 4 h of MLT, as mentioned by *Posch et al.*, [2007]; 5° in latitude and less than 30° in  
421 longitude, as mentioned by *Parkhomov and Rakhmatulin*, [1975]) For these extended distributions, only  
422 the brightest auroral onsets can be associated with Pi1B observations at more than 5° in latitude and 2 h  
423 in MLT distance. Their onsets have been seen to occur earlier at the auroral zone latitude at magnetic  
424 midnight. The horizontal ducting of wave power has been put forward, as well as the westward delay  
425 consistent with the Pi1B and initiated by the westward auroral surge were discussed by *Arnoldy et al.*,  
426 [1998], and the expansion is as rapid as 1 hour (MLT) per ~20 second [*Milling et al.*, 2008]. Currently,  
427 however, there is no report on whether Pi1B waves can expand to the dayside.

428 From both Figure 3 and 4, the maximum correlations here peak around ~8s and exhibit a global property,  
429 although they are strongest around the 15-21 MLT regions. *Lee et al.*, [2001] has shown that impulsive  
430 field-aligned currents are strongly excited near the boundary between magnetospheric cold plasma and  
431 plasma sheet hot plasmas. This corresponds to circumstances when the Alfvén speed undergoes a rapid  
432 variation, and thus intensive shear Alfvén waves can be excited through mode conversion. The indications  
433 here need further analysis to separate the effects of wave propagation and temporal amplitude variation in  
434 order to confirm the behaviour. From these signals, however, we can put forward a possible scenario that  
435 either FMS waves or shear Alfvén waves (which may be generated in the BPS) can propagate to the  
436 ionosphere either obliquely or field aligned, and therefore could be observed by Swarm in addition to the  
437 FACs at all MLT; with the strongest signal centring around 15-21 MLT. We can't confirm, but it is  
438 possible that the Swarm LEO is at just the appropriate altitude for the Pi1B to spread globally and where  
439 dayside waves have not been completely damped. In turn, this may be the cause for the absence of  
440 dayside Pi1B observations in ground based data. This global characteristic observed by Swarm may  
441 broaden our horizon on the association of ULF waves and FACs, as well as the sub-storms. We will  
442 clarify this potential capability in future work.

#### 443 **4 Conclusions**

444 To explore the local time dependence and stability of FACs at Swarm altitudes, we have investigated their  
445 statistical, dual-spacecraft correlation signatures between two Swarm spacecraft, flying side by side from  
446 17<sup>th</sup> Apr. 2014 to 30<sup>th</sup> Apr. 2016, using a method which links the correlation intervals to model estimated  
447 auroral boundaries (after *Xiong and Lühr*, [2014]; *Xiong et al.* [2014]). Thus, the segments are targeted  
448 relative to auroral boundaries defining the limit of current intensity from the ordinary R1 and R2 current  
449 systems. The interval between these boundaries is split into intervals most likely to contain R1 and R2  
450 currents respectively. In fact, the R1 intervals cover latitudes which may contain influences from other

451 current systems, for example, Cusp currents (Region 0), NBZ currents, and the R2 intervals may contain  
452 some ordinary region 1 signals and, indeed, some other currents at noon. It is difficult to separate and  
453 distinguish these at the higher latitudes though this analysis. The unfiltered FAC data adopted here is the  
454 official Level-2 FAC data of Swarm which is obtained by using single-spacecraft methods, which assume  
455 an infinite current sheet approximation can be applied locally to each spacecraft in the manner detailed by  
456 [Ritter *et al.*, 2013]. We have then applied 20 and 60 seconds filtering to yield the low-pass filtered data  
457 and indicate the large-scale FACs (150/450 km along orbit). Cross-correlations are performed mainly on  
458 data obtained from the Swarm A and C spacecraft. The results show that the maximum correlations  
459 obtained from sliding data segments show clear trends in MLT. By connecting the average mid-positions  
460 of the two intervals from Swarm A and C used to estimate the maximum correlations, we show the  
461 current sheet orientation for LEO altitude directly for the first time. It is obvious that the large-scale  
462 current sheets closely follow the oval on the dusk-side and are also well consistent with the oval pattern  
463 on the dawn-side and this ordering is consistent with the correlation trends found. The orientations are  
464 estimated using a high (0.97) correlation level. It was noted that setting lower correlation thresholds for  
465 the current sheet orientations will introduce more influences from small-scale currents.

466 The results show that the R2 currents (referring to all FAC signatures at latitudes in the lower auroral  
467 boundary as defined by Xiong and Lühr [2014]) show the strongest correlations for a broad range of  
468 MLT, centred on pre-dawn and post-dusk, with a higher correlation coefficient on the dusk-side and  
469 lower correlations near noon and midnight. This is consistent with the results for the current sheet  
470 alignments, where the ordering relative to the auroral oval is strongest at lower latitudes and strongest on  
471 the dusk side. The FAC profiles are very sensitive to shifts in longitude, especially for the unfiltered data,  
472 which can be attributed to the lower applicability of the infinite current sheet approximation to the small-  
473 scale currents [Forsyth *et al.*, 2017]. Correlations are much higher for the filtered data and are more stable  
474 for up to 0.3 minutes, i.e. 20 seconds, time difference ( $\delta t$ ) between Swarm A and C. It thus reflects the  
475 predominantly large-scale dominance of R2 FACs and little influence from the small-scale currents in this  
476 region. In contrast, the R1 currents (actually all high latitude currents) peak mainly at the dawn and dusk  
477 side, and are maintained for a shorter range of  $\delta t$ , consistent with the expectation that R1 currents are  
478 more temporally variable.

479 Evidence is also found for the influence from other current systems such as Region 0 and NBZ currents in  
480 the R1 region. Correlations between spacecraft A-B and B-C show little  $\delta t$  or  $\delta lon$  sensitivity, despite  
481 persistent variabilities below 44 minutes, down to 0 minutes. This may be because of the influence from  
482 different altitudes of each spacecraft, i.e. 470km, versus 531km, which compete with the  $\delta t$  or  $\delta lon$   
483 sensitivity. However, another possibility is the temporal stability of the large-scale FACs R1/2 FACs.

484 To test the influence from geomagnetic activity, however, the data has been separated into two segments  
485 (AE index below 110 nT and above 110 nT, with nearly the same data number in each segment).  
486 However, the behaviour is very similar, where the only obvious effect is that the correlations are higher  
487 during geomagnetic activated time. This result is not shown here.

488 The evidence further suggests that the higher latitude FACs are modulated by ULF waves, which seem to  
489 be Pi1B waves in the Alfvén mode with a frequency of  $\sim 8$  seconds. The trends are prominent for the  
490 unfiltered data set, indicating a relationship between the small-scale currents and the Pi1B waves.  
491 However, secondary harmonic waves seem to appear for the 60s filtered FAC data. This analysis  
492 illustrates a new way to reveal pulse observations using LEO satellites. This result arises from a statistical  
493 study and is hard to be found from case-by-case studies because of the fast motion of the LEO satellites.  
494 However, more work needs to be done to clarify this result.

495 The methodology, based on the correlation of single spacecraft estimates, was deliberately chosen to  
496 highlight the locations of small-scale influences, where these add to the larger scale trends. Generally  
497 speaking, therefore, this study clearly reflects the two different domains of FACs: small-scale (some tens  
498 of km) which are time variable and large-scale ( $>100$  km) which are rather stationary. The study is very

499 supportive of the dual-SC FAC approach introduced by Ritter et al and explored recently by others (e.g.  
 500 *Dunlop et al.*, 2015b). The study suggests the time shifts and filters used in multi spacecraft techniques  
 501 are generally suitable for accurate determination of the FACs and perhaps allows the conditions where  
 502 these break down to be further investigated. The evidence further suggests that the higher latitude FACs  
 503 are modulated by ULF waves, which seem to be Pi1B waves in the Alfvén mode with a frequency of ~8  
 504 seconds. The trends are prominent for the unfiltered data set, indicating a relationship between the small-  
 505 scale currents and the Pi1B waves. However, secondary harmonic waves seem to appear for the 60s  
 506 filtered FAC data. This analysis illustrates a new way to reveal pulse observations using LEO satellites.  
 507 This result arises from a statistical study and is hard to be found from case-by-case studies because of the  
 508 fast motion of the LEO satellites. However, more work needs to be done to clarify this result.

## 509 **Acknowledgments**

510 We thank the ESA Swarm project for provision of the data used here. This work is supported by the  
 511 NSFC grants 41431071, 41574155, 40904042, 973 program 2011CB811404 and NERC grant  
 512 NE/H004076/1. MWD is partly supported by STFC in-house research grant. This work is partly  
 513 supported through the ISSI Team ‘Field-Aligned Currents: Their Morphology, Evolution, Source Regions  
 514 and Generators’. We thank the International Space Science Institute in Bern, Switzerland, its staff and  
 515 directors. We also thank Yiqun Yu for the editing of the manuscript.

## 516 **References**

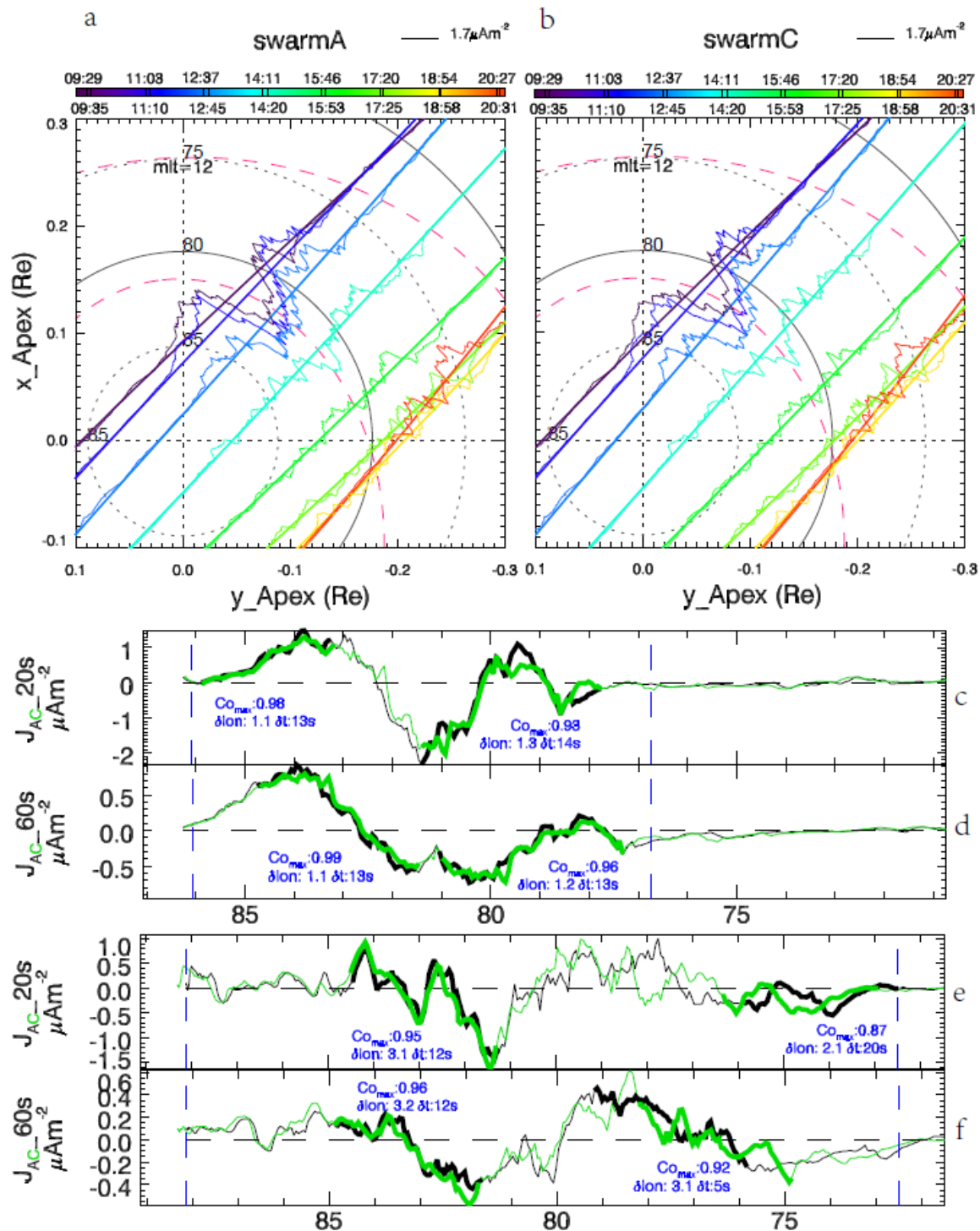
- 517 Anderson, H. R., and R. R. Vondrak (1975), Observations of Birkeland currents at auroral latitudes, *Rev.*  
 518 *Geophys.*, 13(1), 243–262, doi:10.1029/RG013i001p00243.
- 519 Anderson, B. J., K. Takahashi, and B. A. Toth (2000), Sensing global Birkeland currents with iridium@  
 520 engineering magnetometer data, *Geophys. Res. Lett.*, 27, 4045–4048, 10.1029/2000GL000094.
- 521 Arnoldy, R. L., J. L. Posch, M. J. Engebretson, H. Fukunishi, and H. J. Singer (1998), Pi1 magnetic  
 522 pulsations in space and at high latitudes on the ground, *J. Geophys. Res.*, 103(A10), 23581–23591,  
 523 doi:10.1029/98JA01917.
- 524 Bösinger T., U. Wedeken (1987) , Pi1B type magnetic pulsations simultaneously observed at mid and high  
 525 latitudes, *Journal of Atmospheric and Terrestrial Physics*, 49(6), 573-598, 10.1016/0021-  
 526 9169(87)90072-9.
- 527 Bösinger, T., K. Alanko, J. Kangas, H. Opgenoorth, and W. Baumjohann (1981), Correlation between PiB  
 528 type magnetic micropulsations, auroras and equivalent current structures during two isolated substorms,  
 529 *J. Atmos. Terr. Phys.*, 43, 933.
- 530 Bythrow, P. F., T. A. Potemra, R. E. Erlandson, L. J. Zanetti, and D. M. Klumpar (1988), Birkeland  
 531 currents and charged particles in the high-latitude prenoon region: A new interpretation, *J. Geophys.*  
 532 *Res.*, 93(A9), 9791–9803, doi:10.1029/JA093iA09p09791.
- 533 Cao, J., et al. (2008), Characteristics of middle- to low-latitude Pi2 excited by bursty bulk flows, *J.*  
 534 *Geophys. Res.*, 113, A07S15, doi:10.1029/2007JA012629.
- 535 Cao, J.-B., et al. (2010), Geomagnetic signatures of current wedge produced by fast flows in a plasma  
 536 sheet, *J. Geophys. Res.*, 115, A08205, doi:10.1029/2009JA014891.
- 537 Danielides, M. A., S. Shalimov, and J. Kangas (2001), Estimates of the field-aligned current density in  
 538 current-carrying filaments using auroral zone ground-based observations, *Ann Geophys*, 19(7), 699-706,  
 539 doi.org/10.5194/angeo-19-699-2001.
- 540 Dunlop, M. W., D. J. Southwood, K.-H. Glassmeier, and F. M. Neubauer (1988), Analysis of multipoint  
 541 magnetometer data, *Adv. Space Res.*, 8, 273–277, doi:10.1016/0273-1177(88)90141-X.
- 542 Dunlop, M. W., J.-Y. Yang, Y.-Y. Yang, C. Xiong, H. Lüher, Y. V. Bogdanova, C. Shen, N. Olsen, Q.-H.  
 543 Zhang, J.-B. Cao, H.-S. Fu, W.-L. Liu, C. M. Carr, P. Ritter, A. Masson, and R. Haegmans (2015a),

- 544 Simultaneous field-aligned currents at Swarm and Cluster satellites. *Geophys. Res. Lett.*, 42, 3683–3691.  
545 doi: 10.1002/2015GL063738.
- 546 Dunlop, M. W., Y.-Y. Yang, J.-Y. Yang, H. Lühr, C. Shen, N. Olsen, P. Ritter, Q.-H. Zhang, J.-B. Cao, H.-  
547 S. Fu, et al. (2015b), Multispacecraft current estimates at swarm, *J. Geophys. Res. Space*  
548 *Physics*, 120, 8307–8316, doi:10.1002/2015JA021707.
- 549 Dunlop, M. W., S. Haaland, P. C. Escoubet, and X.-C. Dong (2016), Commentary on accessing 3-D  
550 currents in space: Experiences from Cluster, *J. Geophys. Res. Space Physics*, 121, 7881–7886,  
551 doi:10.1002/2016JA022668.
- 552 Dunlop, M. W., S. Haaland, X.-C. Dong, H. Middleton, P. Escoubet, Y.-Y. Yang, Q.-H. Zhang, J.-K. Shi and  
553 C.T. Russell (2008), Multi-point analysis of current structures and applications: Curlometer technique,  
554 in *Electric Currents in Geospace and Beyond* (eds A. Keiling, O. Marghitu, and M. Wheatland), John  
555 Wiley & Sons, Inc, Hoboken, N.J., AGU books, 2018, doi: 10.1002/9781119324522.ch4.
- 556 Forsyth, C., I. J. Rae, I. R. Mann, and I. P. Pakhotin (2017), Identifying intervals of temporally invariant  
557 field-aligned currents from Swarm: Assessing the validity of single-spacecraft methods, *J. Geophys.*  
558 *Res. Space Physics*, 122, 3411–3419, doi:10.1002/2016JA023708.
- 559 Foster, J. C., J.-P. St.-Maurice, and V. J. Abreu (1983), Joule heating at high latitudes, *J. Geophys. Res.*,  
560 88(A6), 4885–4897, doi:10.1029/JA088iA06p04885.
- 561 Friis-Christensen, E., H. Lühr, D. Knudsen and R. Haagmans (2008), Swarm – An Earth Observation  
562 Mission investigating Geospace, *Advances in Space Research*, 41, 210-216  
563 doi:10.1016/j.asr.2006.10.008.
- 564 Fukushima, N. (1976). Generalized theorem for no ground magnetic effect of vertical currents connected  
565 with pedersen currents in the uniform-conductivity ionosphere. *Report of Ionosphere & Space Research*  
566 *in Japan*, 30(30), 35-40.
- 567 Haldoupis, C. I., E. Nielsen, J. A. Holtet, A. Egeland, and H. A. Chivers (1982), Radar auroral  
568 observations during a burst of irregular magnetic pulsations, *J. Geophys. Res.*, 87(A3), 1541–1550,  
569 doi:10.1029/JA087iA03p01541.
- 570 Harang, L. (1946), The mean field of disturbance of polar geomagnetic storms, *Terr. Magn. Atmos.*  
571 *Electr.*, 51(3), 353–380, doi:10.1029/TE051i003p00353.
- 572 Heacock, R. R. (1967), Two subtypes of type Pi micropulsations, *J. Geophys. Res.*, 72(15), 3905–3917,  
573 doi:10.1029/JZ072i015p03905.
- 574 Iijima, T., and T. A. Potemra (1976a), The amplitude distribution of field-aligned currents at northern high  
575 latitudes observed by Triad, *J. Geophys. Res.*, 81(13), 2165–2174, doi:10.1029/JA081i013p02165.
- 576 Iijima, T., and T. A. Potemra (1976b), Field-aligned currents in the dayside cusp observed by Triad, *J.*  
577 *Geophys. Res.*, 81(34), 5971–5979, doi:10.1029/JA081i034p05971.
- 578 Iijima, T., and T. A. Potemra (1978), Large-scale characteristics of field-aligned currents associated with  
579 substorms, *J. Geophys. Res.*, 83(A2), 599–615, doi:10.1029/JA083iA02p00599.
- 580 Iijima, T., T. A. Potemra, L. J. Zanetti, and P. F. Bythrow (1984), Large-scale Birkeland currents in the  
581 dayside polar region during strongly northward IMF: A new Birkeland current system, *J. Geophys. Res.*,  
582 89(A9), 7441–7452, doi:10.1029/JA089iA09p07441.
- 583 Gjerloev, J. W., and R. A. Hoffman (2014), The large-scale current system during auroral substorms, *J.*  
584 *Geophys. Res. Space Physics*, 119, 4591–4606, doi:10.1002/2013JA019176.
- 585 Gjerloev, J.W., S. Ohtani, T. Iijima, B. Anderson, J. Slavin, and G. Le, (2011), Characteristics of the  
586 terrestrial field-aligned current system, *Ann. Geophys.*, 29, 1713–1729, doi:10.5194/angeo-29-1713-  
587 2011.

- 588 Korth, H., Y. Zhang, B. J. Anderson, T. Sotirelis, and C. L. Waters (2014), Statistical relationship between  
589 large-scale upward field-aligned currents and electron precipitation, *Journal of Geophysical Research:*  
590 *Space Physics*, 119 (8), 2014JA019961, doi:10.1002/2014JA019961.
- 591 Lessard, M. R., E. J. Lund, S. L. Jones, R. L. Arnoldy, J. L. Posch, M. J. Engebretson, and K. Hayashi  
592 (2006), Nature of Pi1B pulsations as inferred from ground and satellite observations, *Geophys. Res.*  
593 *Let.*, 33, L14108, doi:10.1029/2006GL026411.
- 594 Lessard, M. R., E. J. Lund, H. M. Kim, M. J. Engebretson, and K. Hayashi (2011), Pi1B pulsations as a  
595 possible driver of Alfvénic aurora at substorm onset, *J. Geophys. Res.*, 116, A06203,  
596 doi:10.1029/2010JA015776.
- 597 Liu, W., T. E. Sarris, X. Li, S. R. Elkington, R. Ergun, V. Angelopoulos, J. Bonnell, and K. H. Glassmeier  
598 (2009), Electric and magnetic field observations of Pc4 and Pc5 pulsations in the inner magnetosphere:  
599 A statistical study, *J. Geophys. Res.*, 114, A12206, doi:10.1029/2009JA014243.
- 600 Lu, G., et al. (1998), Global energy deposition during the January 1997 magnetic cloud event, *J. Geophys.*  
601 *Res.*, 103(A6), 11685–11694, doi:10.1029/98JA00897.
- 602 Lühr, H., J. F., Warnecke, M. K. A., Rother (1996), An algorithm for estimating field-aligned currents  
603 from single spacecraft magnetic field measurements: a diagnostic tool applied to Freja satellite data,  
604 *IEEE Trans. Geoscience and Remote Sensing*, 34(6), 1369-1376.
- 605 Lühr, H., J. Park, J. W. Gjerloev, J. Rauberg, I. Michaelis, J. M. G. Merayo, and P. Brauer (2015), Field-  
606 aligned currents' scale analysis performed with the Swarm constellation, *Geophys. Res. Let.*, 42,  
607 doi:10.1002/2014GL062453.
- 608 Ma, Z. W., L. C. Lee, A. Otto (1995), Generation of field-aligned currents and Alfvén waves by 3D  
609 magnetic reconnection, *Geophys. Res. Space Physics*, 22, 1737-1740,  
610 doi:10.1029/95GL01430. McDiarmid, I. B., J. R. Burrows, Margaret D. Wilson (1980), Comparison of  
611 magnetic field perturbations and solar electron profiles in the polar cap, *J. Geophys. Res.*, 85(A3), 1163–  
612 1170, doi: 10.1029/JA085iA03p01163.
- 613 Marshall, J. A., J. L. Burch, J. R. Kan, P. H. Reiff, J. A. Slavin (1991), Sources of field-aligned currents in  
614 the auroral plasma, *J. Geophys. Res.*, 18, 45–48, doi:10.1029/90GL02674.
- 615 McGranaghan, R., D. J. Knipp, T. Matsuo, and E. Cousins (2016), Optimal interpolation analysis of high-  
616 latitude ionospheric Hall and Pedersen conductivities: Application to assimilative ionospheric  
617 electrodynamics reconstruction, *J. Geophys. Res. Space Physics*, 121, 4898–4923,  
618 doi:10.1002/2016JA022486.
- 619 McGranaghan, R. M., Mannucci, A. J., & Forsyth, C. (2017). A comprehensive analysis of multiscale  
620 field-aligned currents: Characteristics, controlling parameters, and relationships. *Journal of*  
621 *Geophysical Research: Space Physics*, 122, 11,931–11,960, doi:10.1002/2017JA024742
- 622 Merkin, V. G., J. G. Lyon, and S. G. Claudepierre (2013), Kelvin-Helmholtz instability of the  
623 magnetospheric boundary in a three-dimensional global MHD simulation during northward IMF  
624 conditions, *J. Geophys. Res. Space Physics*, 118, 5478–5496, doi:10.1002/jgra.50520.
- 625 Milling, D. K., I. J. Rae, I. R. Mann, K. R. Murphy, A. Kale, C. T. Russell, V. Angelopoulos, and S.  
626 Mende (2008), Ionospheric localisation and expansion of long-period Pi1 pulsations at substorm onset,  
627 *Geophys. Res. Let.*, 35, L17S20, doi:10.1029/2008GL033672.
- 628 Neubert, T., and F. Christiansen (2003), Small-scale, field-aligned currents at the top- side ionosphere,  
629 *Geophys. Res. Let.*, 30, 2010, doi:10.1029/2003GL017808, 19
- 630 Newell, P. T., T. Sotirelis, and S. Wing (2009), Diffuse, monoenergetic, and broadband aurora: The global  
631 precipitation budget, *J. Geophys. Res.*, 114, A09207, doi:10.1029/2009JA014326.
- 632 Rankin, R., J. C. Samson, and V. T. Tikhonchuk (1999), Discrete Auroral Arcs and Nonlinear Dispersive  
633 Field Line Resonances, *Geophys Res Lett*, 26(6), 663-666, doi:10.1029/1999GL900058.

- 634 Ritter, P., Lühr, H., & Rauberg, J. (2013). Determining field-aligned currents with the Swarm constellation  
635 mission. *Earth, Planets and Space*, 65(11), 9. <https://doi.org/10.5047/eps.2013.09.006>.
- 636 Parkhomov, V.A., Rakhmatulin, R.A. (1975), Localization and Drift of Pi1B Source (Issledovaniya po  
637 geomagnetizmu, aeronomii i fizike Solntsa), Vol. 36. Nauka, Moscow, pp. 131–137 (in Russian).
- 638 Pilipenko, V. A., N. G. Mazur, E. N. Fedorov, and M. J. Engebretson (2008), Interaction of propagating  
639 magnetosonic and Alfvén waves in a longitudinally inhomogeneous plasma, *J. Geophys. Res.*, 113,  
640 A08218, doi:10.1029/2007JA012651.
- 641 Pitout, F., P. Eglitis, and P.-L. Blelly (2003), High-latitude dayside ionosphere response to Pc5 field line  
642 resonance, *Ann. Geophys.*, 21, 1509–1520, doi: 10.5194/angeo-21-1509-2003.
- 643 Pitout, F., A. Marchaudon, P.-L. Blelly, X. Bai, F. Forme, S. C. Buchert, and D. A. Lorentzen (2015),  
644 Swarm and ESR observations of the ionospheric response to a field-aligned current system in the high-  
645 latitude midnight sector, *Geophys. Res. Lett.*, 42, doi:10.1002/2015GL064231.
- 646 Posch, J. L., M. J. Engebretson, S. B. Mende, H. U. Frey, R. L. Arnoldy, M. R. Lessard, L. J. Lanzerotti, J.  
647 Watermann, M. B. Moldwin, and P. V. Ponomarenko (2007), Statistical observations of spatial  
648 characteristics of Pi1B pulsations, *J Atmos Sol-Terr Phy*, 69(15), 1775-1796,  
649 doi:10.1016/j.jastp.2007.07.015.
- 650 Richmond, A. D.(1995), Ionospheric electrodynamics using magnetic apex coordinates, *J. Geomag.*  
651 *Geoelectr.*, 47(2), 191–212, doi: 10.5636/jgg.47.191.
- 652 Sonnerup, B. U. Ö., and M. Scheible (1998), Minimum and maximum variance analysis, ISSI Scientific  
653 Reports Series, 1, 185–220.
- 654 Stasiewicz, K., et al. (2000), Small-scale Alfvénic structure in the aurora, *Space Sci. Rev.*, 92, 423–533,  
655 doi:10.1023/A:1005207202143.
- 656 Stolle, C., Floberghagen, R., Lühr, H., Maus, S., Knudsen, D. J., Alken, P.,...Visser, P. N.(2013). Space  
657 Weather opportunities from the Swarm mission including near real time applications. *Earth Planets and*  
658 *Space*, 65(11), 17, doi:10.5047/eps.2013.10.002.
- 659 Waters, C. L., and M. D. Sciffer (2008), Field line resonant frequencies and ionospheric conductance:  
660 Results from a 2-D MHD model, *J. Geophys. Res.*, 113, A05219, doi:10.1029/2007JA012822.
- 661 Wing, S., M. Gkioulidou, J. R. Johnson, P. T. Newell, and C.-P. Wang (2013), Auroral particle  
662 precipitation characterized by the substorm cycle, *J. Geophys. Res. Space Physics*, 118, 1022–1039,  
663 doi:10.1002/jgra.50160.
- 664 Wing, S., D. H. Fairfield, J. R. Johnson, and Shin-I. Ohtani (2015), On the field-aligned electric field in the  
665 polar cap, *Geophys. Res. Lett.*, 42, 5090–5099, doi:10.1002/2015GL064229.
- 666 Xiong, C. and H. Lühr (2014), An empirical model of the auroral oval derived from CHAMP field-aligned  
667 current signatures – Part 2, *Ann. Geophys.*, 32, 623–631, 2014, doi:10.5194/angeo-32-623-2014.
- 668 Xiong, C., H. Lühr, H. Wang, and M.G. Johnsen (2014), Determining the boundaries of the auroral oval  
669 from CHAMP field-aligned currents signatures – Part 1, *Ann. Geophys.*, 32, 609–622, 2014,  
670 doi:10.5194/angeo-32-609-2014.
- 671 Yu, Y., A. J. Ridley, D. T. Welling, and G. Tóth (2010), Including gap region field-aligned currents and  
672 magnetospheric currents in the MHD calculation of ground-based magnetic field perturbations, *J.*  
673 *Geophys. Res.*, 115, A08207, doi:10.1029/2009JA014869.
- 674 Yu, Y., J. Cao, H. Fu, H. Lu, and Z. Yao (2017), The effects of bursty bulk flows on global-scale current  
675 systems, *J. Geophys. Res. Space Physics*, 122, 6139–6149, doi:10.1002/2017JA024168.
- 676 Zmuda, A. J., J. H. Martin, and F. T. Heuring (1966), Transverse magnetic disturbances at 1100 kilometers  
677 in the auroral region, *J. Geophys. Res.*, 71(21), 5033–5045, doi:10.1029/JZ071i021p05033.

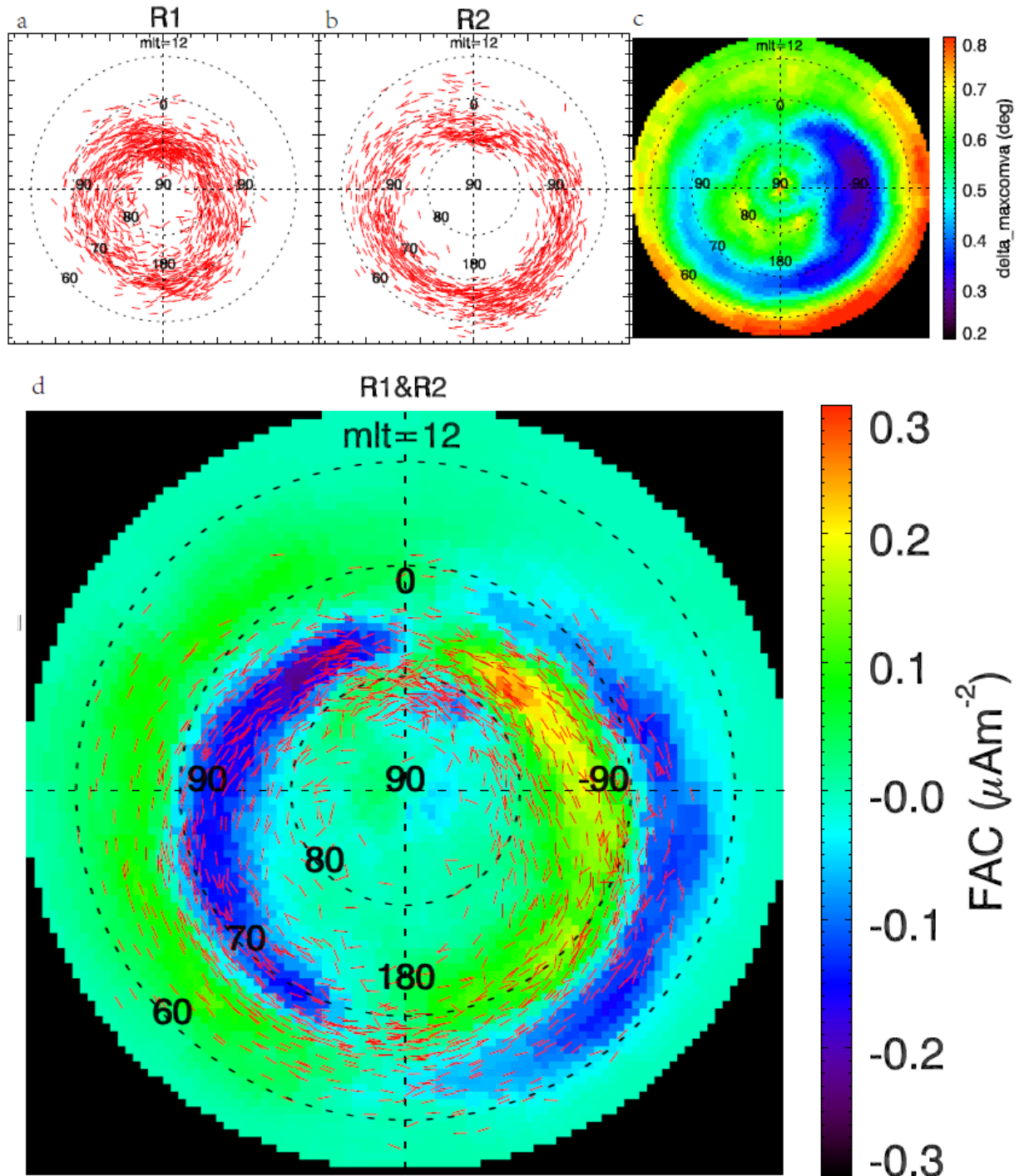
678 Zmuda, A. J., F. T. Heuring, and J. H. Martin (1967), Dayside magnetic disturbances at 1100 kilometers in  
 679 the auroral oval, *J. Geophys. Res.*, 72(3), 1115–1117, doi:10.1029/JZ072i003p01115.



680

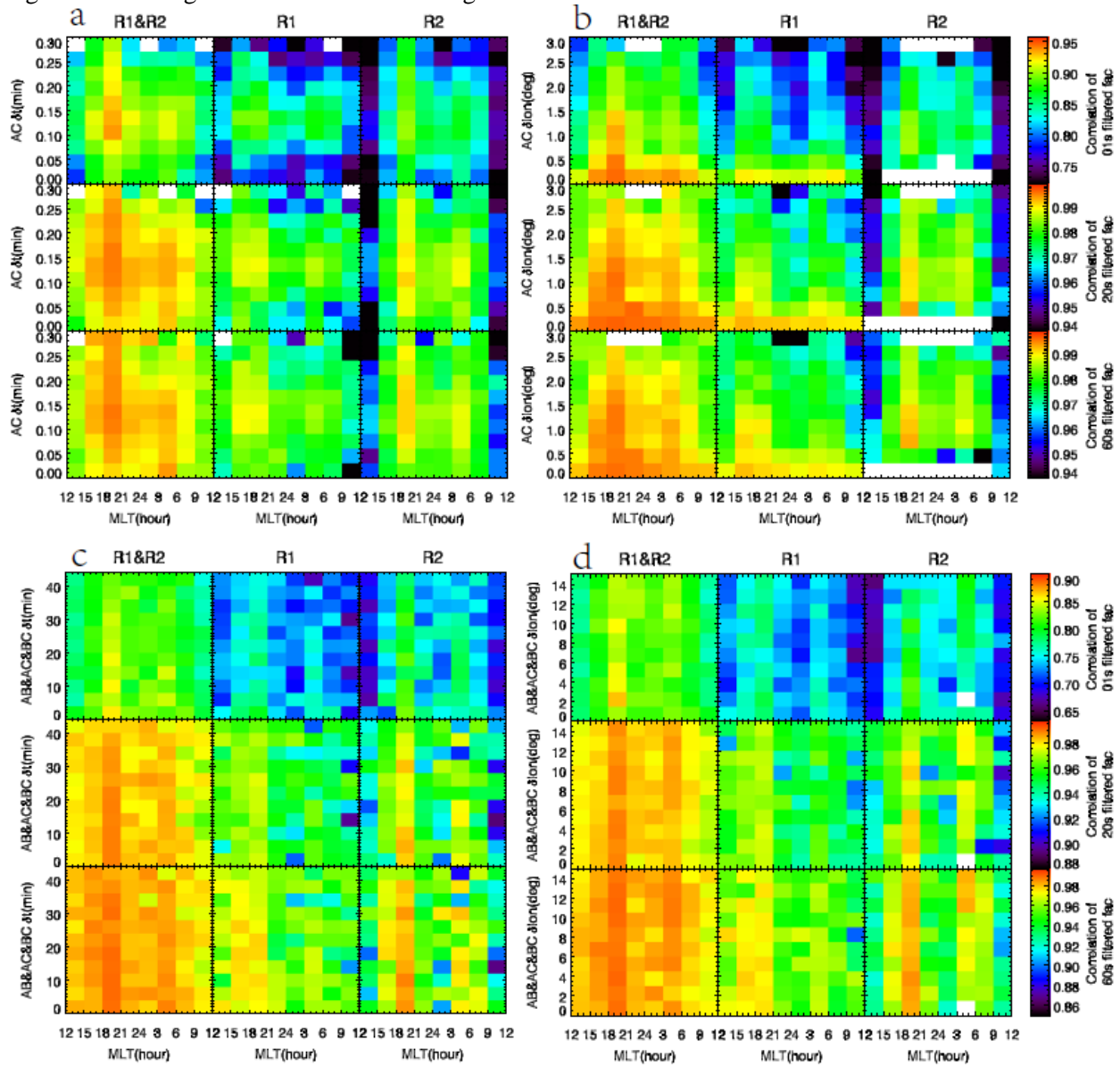
681 **Figure 1:** Swarm A/C FACs for an example interval on 6<sup>th</sup>, June, 2014, corresponding to a sequence of  
 682 consecutive orbits (colour coded with time from black to red shown above the colour bar in a) and b),  
 683 where: a) shows 20s filtered FACs observed by Swarm A plotted on the orbits within time period 09:29-  
 684 20:31 UT where the FAC magnitude scale is denoted on the top-right, and b) shows the same as a) but for

685 Swarm C. The model [*Xiong and Lühr, 2014*] poleward and equatorward auroral boundaries of current  
686 intensity on 14:30 UT are shown on Figure 1 (**a, b**) by the magenta dashed curves. The lower panels (**c** to  
687 **f**) show two, dual spacecraft (Swarm A (black) and Swarm C (green)) intervals within this sequence,  
688 plotted as a function of APEX latitude, and the current value not on the same scale: **c** and **d**) show the  
689 first north descending orbit track (black orbit in panels **a** and **b**), where the R1 and R2 boundaries are  
690 estimated to be at 9:30 and 9:33 UT, and **e**) and **f**) are for three orbits later (light blue orbit in panels **a** and  
691 **b**) with boundaries at 14:13 and 14:18 UT. Each pair shows the 20s (upper panels, **c** and **e**) and 60s (lower  
692 panels, **d** and **f**) moving average data and also indicates the sliding maximum correlation achieved for the  
693 two intervals between R1 and R2 boundaries (blue dashed lines) with the longitude and time shift  
694 between A and C for each interval (blue text).  
695

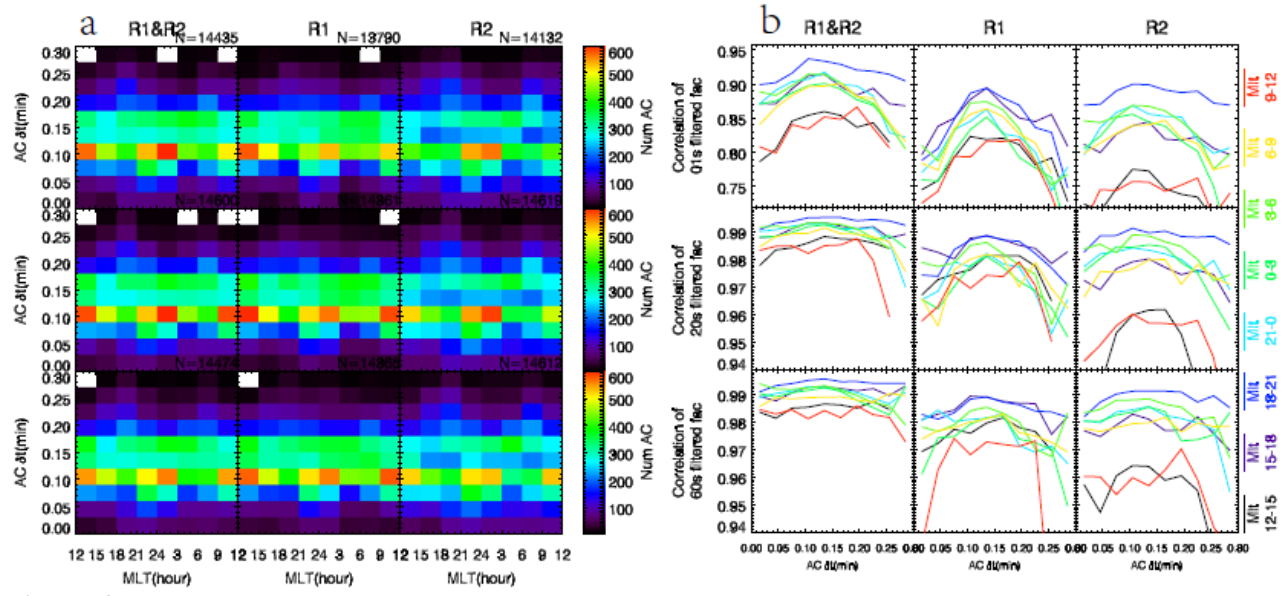


696  
 697 **Figure 2:** **a, b)** Northern hemisphere polar map, showing inferred current sheets, for Swarm A and C  
 698 data from 17<sup>th</sup> Apr. 2014 to 20<sup>th</sup> Aug. 2014, during which time Swarm A and C's orbit has covered 24hrs  
 699 MLT. These are plotted using lines of normalised length which connect the average Swarm A and C  
 700 positions of those orbit segments producing the maximum correlations (drawn for 20 seconds filtered  
 701 data), where: **a)** shows the current sheet orientations found for the higher latitude regions, **b)** shows those  
 702 for the lower latitude regions, **c)** shows the intersection angle of current sheets calculated by maximum  
 703 correlation and MVA method, for Swarm A and C data from 17<sup>th</sup> Apr. 2014 to 30<sup>th</sup> Apr. 2016 and **d)**  
 704 shows a Northern hemisphere polar map, showing the average FACs for Swarm A and C data from 17<sup>th</sup>

705 Apr. 2014 to 30<sup>th</sup> Apr. 2016, overlain with similar current sheet orientations to **a**) and **b**) but for both  
 706 higher latitude regions and lower latitude regions.



707 **Figure 3:** **a**) nine panels showing vertically from the top the A-C correlation, binned with the  $\delta t$   
 708 difference, as a function of MLT, for unfiltered data, 20 seconds low pass filtered data and 60 seconds  
 709 low pass filtered data. The three columns are for correlations over the whole interval between the R1 and  
 710 R2 boundaries and for the intervals covering R1 and R2 respectively (denoted by R1&R2, R1 and R2  
 711 each at the top); **b**) similar array of correlations but binned with  $\delta lon$ ; **c**, **d**) similar array of correlations  
 712 but of A-B and B-C correlation.  
 713



714  
715  
716  
717

**Figure 4:** a) number of cases in each bin of Figure 3a, and b) similar information to that in Figure 3a but correlations are indicated by the y axis on the left of each panel, here different colours represent different MLTs and the  $\delta t$  difference is now shown by the x axis.

Figure 1.

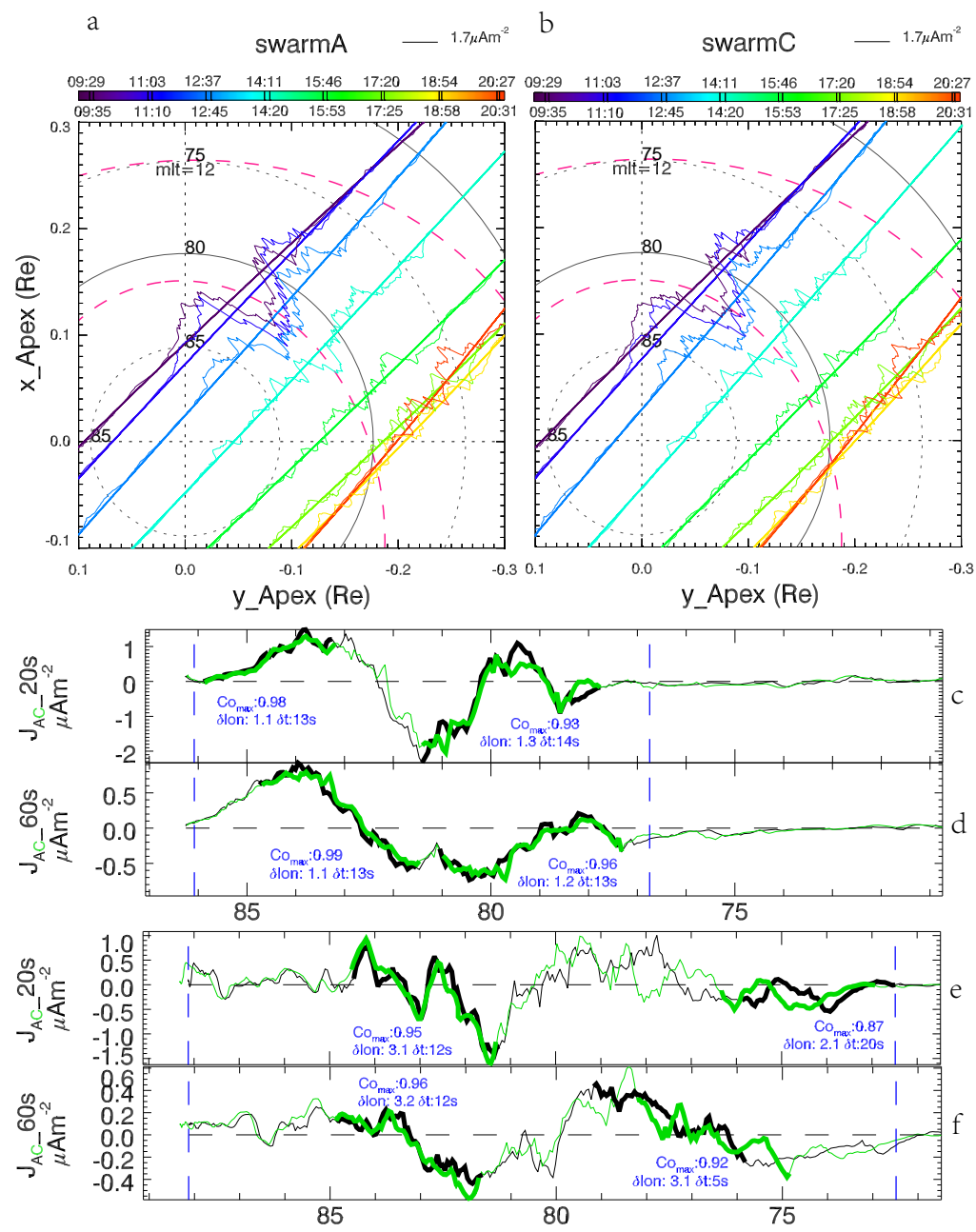


Figure 2.

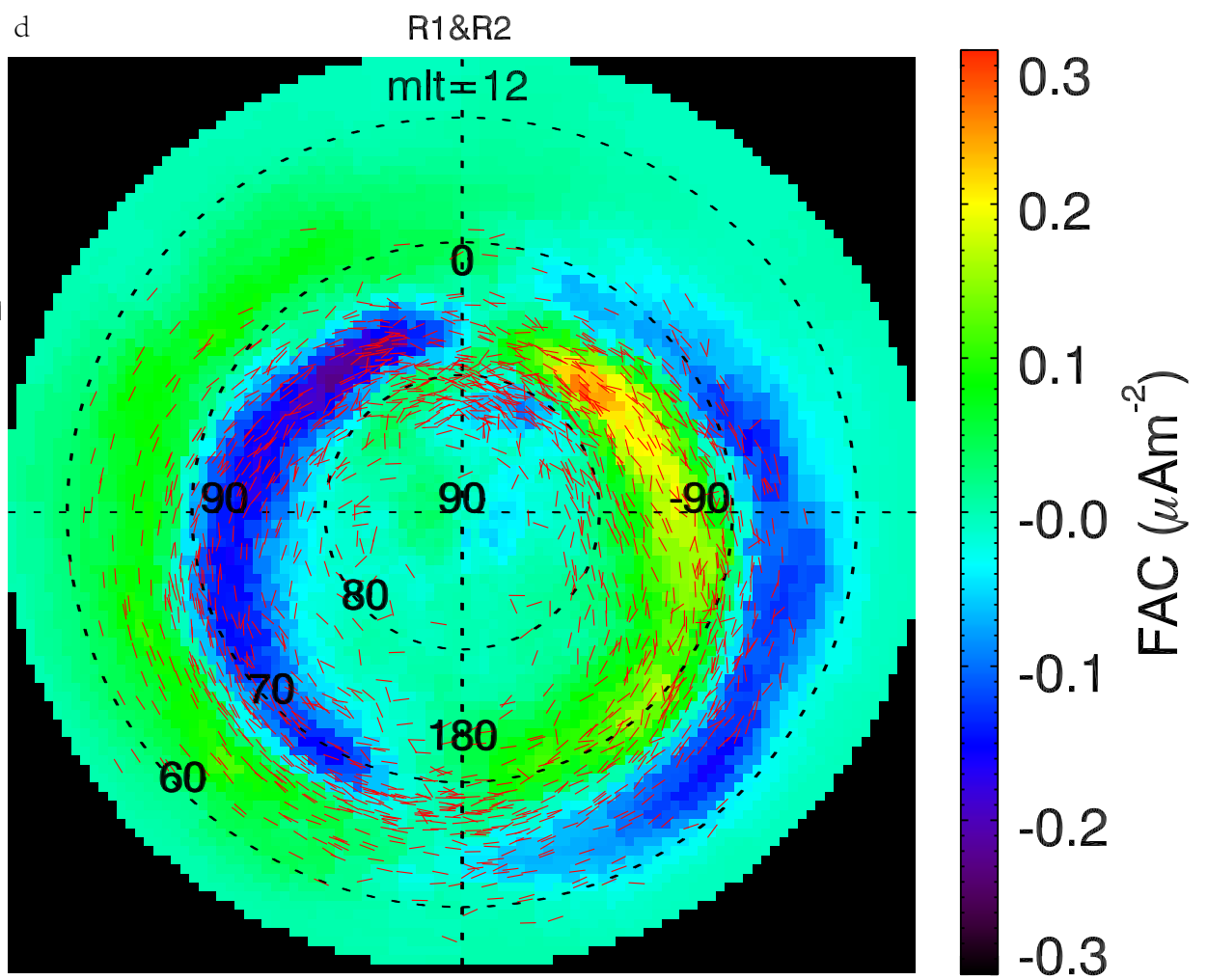
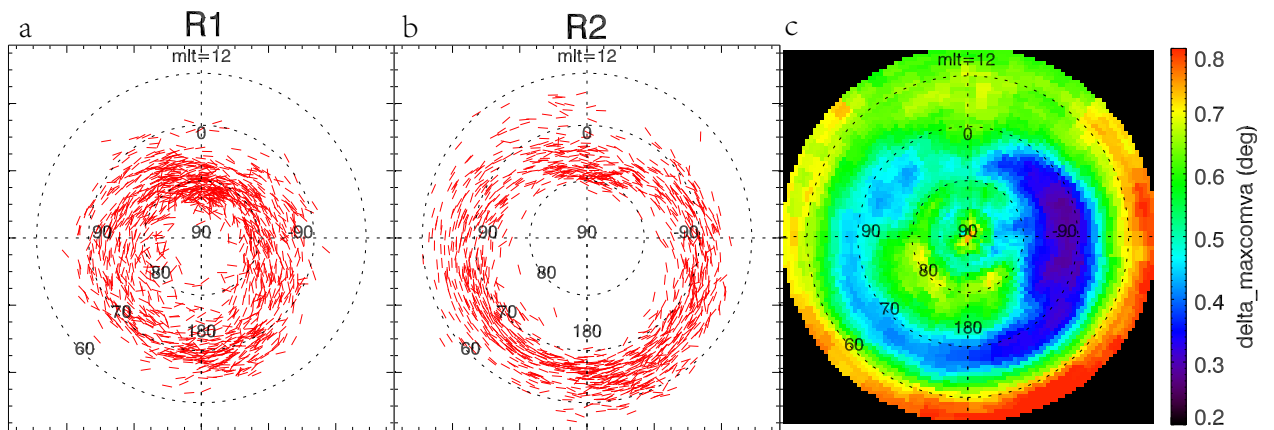
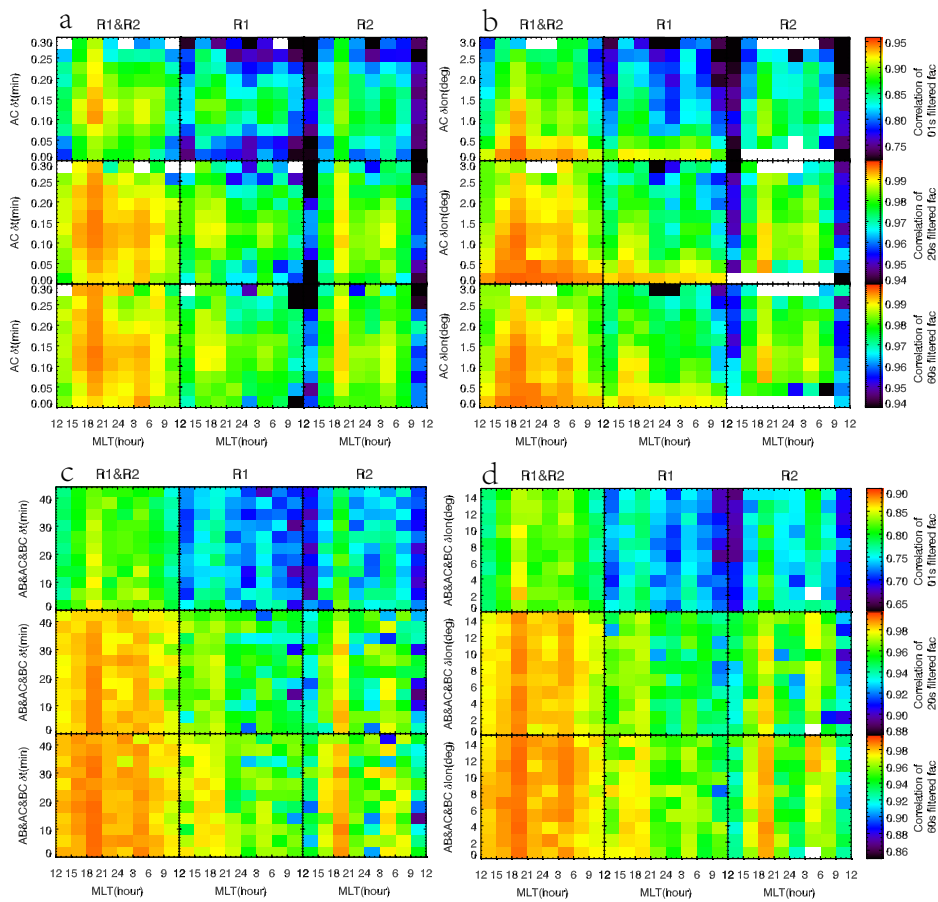


Figure 3.



**Figure 4.**

